3D Reconstruction based on NIR single-pixel for drone navigation under rainy condition

Carlos A. Osorio Quero*, Daniel Durini, Jose Rangel-Magdaleno, Jose Martinez-Carranza and Ruben Ramos-Garcia
Instituto Nacional de Astrofísica, Óptica y Electrónica (INAOE), 72840, Mexico

ABSTRACT

In recent years, 3D reconstruction has become a challenging task for navigation systems. Therefore, different technologies such as RGB cameras, LIDARs, or RADAR can capture information from the environment and perform 3D reconstruction. In an environment of high dispersion and low illumination, it is necessary to have a robust solution that operates in the infrared spectrum. One solution is to integrate Single-Pixel Near Infra-Red Imaging (SPI-NIR) technology, which allows image reconstruction using few samples and operates in high dispersion conditions. In this work, an evaluation of the performance of an SPI-NIR vision system with active illumination for 3D image reconstruction in rainy environments is performed. The reconstruction of 3D objects is performed from the reconstruction of a low-resolution SPI-NIR 2D image, using a robust unified reflectance model that combines the Lambertian, Oren-Nayar, and Blinn-Phong models to improve the 3D image of objects with surface roughness or with low reflectance. For 3D reconstruction, single-view Shape-From-Shading (SFS) based on fast Eikonal solvers was used. This makes it possible to improve the shape of the 3D object, reduce computation time for future applications and generate real-time 3D images in harsh environments.

1 INTRODUCTION

3D reconstruction is itself a challenging task. There are different type of techniques for the reconstruction as mechanical based on ultrasound [1], and the radiometric classified active through the use of Lidar [2], Time of Flight [2], interferometry [3], structured light projection [4], and passives subdivided into the single-view approaches [5], such as Shape-from-Focus(SFF), shape-from-shading(SFS) and shape-from-texture(SFT), and multi-view approaches [5], such as structure from motion and stereo-vision. The goal of a 3D surface reconstruction is to obtain depth information of an object or its surface topology. In conditions of scattering, this can be a complex task with high computational load. In the case of using RGB sensors, there are some limitations due to susceptibility to weather conditions, including rain, snow, and fog or low-visibility scenario [6]. A solution uses InGaAs sensors that operate in the near-infrared spectrum (NIR) at the wavelength 1550nm, through a system with active illumination to illuminate the surface object and make the 3D reconstruction. The NIR has a better performance in outdoor sceneries with high scattering over Long-wave infrared (LWIR) and the visible (VIS), and it can be adapted by active illumination while LWIR is not possible. However, due to the increasing droplet diameters of water particles, there is an increase in the extinction coefficient β [7] factor related to the loss of path light received for the photodetectors. This effect causes a decrease in the level contrast in the scene that can be reconstructed. In LWIR under the rainy condition, the value β is higher than the NIR spectrum. Therefore, the distance of detection is low, and there is more loss, with that the performance image reconstructed is low quite[8].

This work proposes a vision system 3D image single view based on single-pixel imaging technology that allows the 2D reconstruction using a few samples and the SFS method.The SFS 3D reconstruction method uses a single 2D image for surface reconstruction, from a specific perspective, using the changes of illumination shading to infer the 3D shape of the object,different from SFF and SFT [5] that need to have an image stack the estimate the depth. Currently, there are no reported works about the effects to apply SPI-NIR 3D reconstruction in scattering rain, for which, in this work we focus on single-view method evaluation applying shape-from-shading technique in combination with fast Eikonal solvers method [9]. Starting from a 2D single-pixel NIR low-resolution image, we performed the 3D reconstruction in a controlled scenario that simulates the rainy condition for future object detection applications on in-flight and navigation for unmanned vehicles (UMV).

2 SINGLE-PIXEL OBJECT RECONSTRUCTION

The generation of single-pixel imaging is based on the principle of spatial information modulation from the projection of a sequence of structured patterns of light through light modulation devices such as SLM, DMD, or others (see Fig 1). The object is imaged through a lens system, the intensity of the light reflected and transmitted is collected by a photodiode. The relationship between the structured and reflected light signal measurement can be depicted (1)[4].

*Email address(es): caoq@inaoep.mx

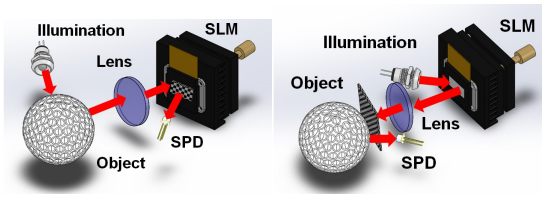

(a) (b)

Figure 1: The two different approaches applied to SPI: a) Front modulation: the object illuminated by a light source and the light reflected by him gets directed through a lens onto an SLM, the light reflected is detected by a photo-detector (or single-pixel detector, SPD). b) Back modulation: the SLM device projects a sequence of patterns and the reflected light is capture by the SPD[4].

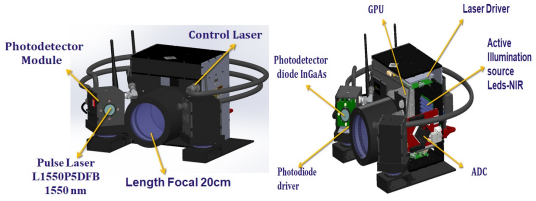

(a) (b)

Figure 2: The proposed vision system dimension is 11x12x13 cm, focal length 20 cm, weight 1.3kg, power consumption 25W, a) first stage module photodiode, active illumination source, photodetector diode InGaAs FGA015, b) second stage GPU unit and ADC[14].

$$S_i = \alpha \sum_{x=1}^{M} \sum_{y=1}^{N} O\,(x,y)\,\Phi_i\,(x,y) \tag{1}$$

Where (x, y) is the spatial coordinate, O denotes object reflectivity, Φ_i is i_{th} structured pattern, S_i is the i_{th} single-pixel measurement corresponding to Φ_i, α is a constant factor depending on the opto-electronic response of the used single-pixel detector, and denotes a point-wise multiplication. The size of both the object and the pattern is M × N pixels, and through the knowledge of the structured patterns and reflected light signal measurement is possible to apply an algorithm to recover the object image. The reconstructed image I is proportional to object reflectivity O. The reconstructed object image can be depicted (2)[4].

$$S_i = \alpha \sum_{x=1}^{M} \sum_{y=1}^{N} I\,(x,y)\,\Phi_i\,(x,y) \tag{2}$$

Where the reconstructed image is expressed as the inner product of the measurements and the structured pattern, the spatial light modulation in single-pixel imaging can be implemented in two different schemes [4], a structured illumination scheme termed front modulation (Fig.1a) and a structured detection scheme termed back modulation (Fig.1b).

2.1 SPI-NIR Vision system test architecture

In this work, We propose a vision system SPI-NIR of the type back modulation (see figure 1b) with an active illumination through a NIR LEDs 8x4 matrix, in the range of the 1550 nm wavelength.The back modulation configuration offers the advantage that light is captured directly by the SPD, and it doesn't need to adapt a light divider and lens internally to concentrate the light over the SPD as front modulation(see figure 1a) with reducing the weight and the complexity of the system.The active illumination offers the capacity to project patterns in low-vision conditions (scenarios with dust, fog, rain, or smoke), increasing the capacity of outdoor operation. Another advantage is the fact that the atmosphere being able to absorb the wavelength between 1500-1600 nm [10], for which our vision system SPI is less sensitive to background noise [11], increasing the range of the detection in outdoor conditions, which gives an operating advantage for future applications as a vision sensor for applications of navigation in unmanned Aerial Vehicle (UAV) (see Fig.3). The SPI-NIR architecture proposed in this work is divided into two stages: the first will control the elements used to generate images through the single-pixel principle: a photo-detector (diode FGA015 @ 1550nm), source light, and ADC (see Fig.2a), and a second stage is the responsible of processing the signal captured by the photo-diode module through the use of an ADC, which is controlled by the GPU unit (see Fig.2b). The GPU unit (Jetson Nano) is also responsible for generating the Hadamard patterns and processing the converted data by the ADC, used by the Batch-OMP[12] algorithm running in the GPU unit to generate the 2D/3D image.To design the vision system, we define some parameters performance for integration as sensor vision for UAVs. In image capture under rainy conditions, we define exposure time as taking one SPI image in 1/50 s, for an aperture to f/2.38 with an exposure value EV=-4 and an ISO of 5000 sensitivity[13], with we can take the image outdoor with low-visibility. Others effect consider in our design is the motion blur <20% , for which we define flight speed maximum between 7.5 m/s to 30m/s for different flight height (see Table.1).

Table 1: Effects of fight height on ground sampling distance (GSD) and fight speed for a motion blur 20% and a shutter speed of 1/50s.

Flight height(m)	10	20	30	40
Flight speed(m/s)	7.5	15	22.5	30
GSD(mm)	0.75	1.5	2.25	3

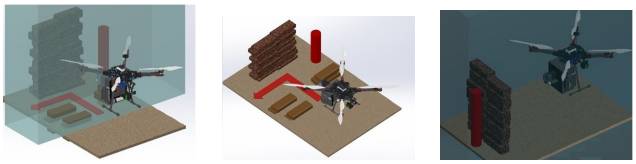

(a) (b) (c)

Figure 3: Vision sensor SPI-NIR for applications in UMV, a) autonomous Navigation in adverse environments, b)obstacle detection, c)3D reconstruction of scenes with low-illumination [14].

3 SCATTERING EFFECT

When light interacts with water particles in the air, various physical phenomena occur as reflection, refraction, absorption, and scattering. This interaction produces dissipation of the photon's energy, the phenomenon is called scattering. The scattering is related to the size particles $sp = 2\pi r/\lambda$ of the particle [15], r being the radius. According to the Rayleigh scattering model, the light scattering strongly dependent on the wavelength and to be inversely proportional to the fourth power of the wavelength [6]. However, the particles in the atmosphere exhibit some different sizes. A more realistic relationship between extinction efficiency and size particle size approximates the probability of scattering to occur when the wavelength of the incident radiation is approximately equal to the particle's radius. Thereby, small particles with a radius less than 1mm scatter mainly in the visible portion of the spectrum, and particles of more significant size scatter stronger in the spectrum IR [6].

3.1 Modeling rain environment

We proposed a rain model adapted to single-pixel to determine the attenuation factor of the source light $\alpha(\lambda, D)$ for different drop sizes and determinate the maximum distance for possible measurements (seen figure 7 Appendix A). The proposed model consisted of three parts, first we define the weather parameters in rain environments as the reflectivity (Reflectivity factor) $Z = \sum N_i D^6$ [16], Z is related with level concentration rain N_o[17], and the differential reflectivity Z_{dr} depend on the rain rate defined as $dBZ_{dr} = 10log(Z_h/Z_v)$ [18], where Z_h horizontal polarized reflectivity [18] and Z_v vertical polarized reflectivity [18]. These parameters depend on drop diameter D, which is given by the Marshall Palmer distribution[19]. In the second part, we considered the Mie scattering effect for which we calculate the scattering efficiency Q_{sca}[20], absorption efficiency Q_{abs} [20], and extinction efficiency Q_{ext} [20] for a particle with diameter D and refractive index m, Q_{abs}[20] is related to an absorption coefficient $\mu_a(\lambda, D)$[20] and ,the third part of the model we considered the rain speed effect [21]. In the rainy condition, the effective measurement range is reduced due to the number of photons $E(N)$[14] impinging the photo-detector photo-active is less, varying the range of measurement from 18 cm to 10 cm for materials with a reflection index of 0.2 and the 28.5 cm to 12.6 cm and, for materials with a reflection index of 0.8 for droplet size $0.5mm$ (seen table 2). This variation in the measurement range caused by scattering should be considered for the 3D reconstruction test.

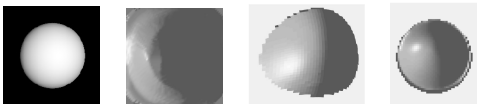

(a) (b) (c) (d)

Figure 4: Generation 3D image through of rectance model, a) 2D image, b)3D image lamberting model, c)3D image Oren-Nayar model,d) 3D image Unified model.

Table 2: Single-pixel maximum measured distance.

Reflection index	0.2	0.5	0.8
Dry maximum distance (cm)	18.4	22.4	24.4
Rain dropping size @3 mm (cm)	16	18	19.6
Rain dropping size @2 mm (cm)	15.6	17.2	18.8
Rain dropping size @1 mm (cm)	14	16	17.2
Rain dropping size @0.5 mm (cm)	10	11.2	12.6

4 REFLECTANCE MODEL

In previous works have been reported different reflectance models, for reconstruction of the 3D image using the method of SFS, as Lambertian [22], Oren–Nayar [23] and Blinn–Phong [24]. Each model has an own feature to be applied for different types of surfaces from smooth to rough or diffuse, for which in this work, we unified a reflectance model through the linear combination of the models previously mentioned.

4.1 Lamberting reflectance model

A Lambertian surface has the property of invariant luminance according to the viewing angle (see Fig.4b). Lambert's law determines how much of the incident light is reflected, which is constant in any direction, which means that the reflected intensity is not dependent on the viewing angle but the light source's orientation relative to the surface is. Therefore, the Lambertian surface is modeled as the light source intensity I_o product, the surface albedo ρ, and the cosine of the angle θ, between source directions S and surface normal N (3)[22]. The Lambertian model is very straightforward and computationally efficient, widely applied in the reconstruction of 3D images.

$$I = \frac{I_o}{\pi}\rho cos(\theta) \tag{3}$$

4.2 Oren–Nayar and Blinn–Phong Reflectance Model

Due to the Lambert model is based on smooth surface reflectance, in diffuse surface conditions, the Oren-Nayar

model improves 3D reconstruction, considered the roughness of the surface as the standard deviation of the Normal Gaussian distribution (see Fig.4c)(4) [23]

$$L_r(\theta_i, \phi_i, \theta_r, \phi_r) = I_o \frac{\rho_d}{\pi} cos\phi_i \, (A + B \, max\,[0, cos\,(\theta_r - \theta_i)]\, sin\alpha tan\beta \quad (4)$$

where $A = 1 - 0.5\sigma^2/\left(\sigma^2 + 0.33\right)$, $B = 0.45\sigma^2/\left(\sigma^2 + 0.09\right)$, $\alpha = max\,[\theta_i, \theta_r]$, $\beta = min\,[\theta_i, \theta_r]$

An improvement of the Oren-Nayar model is the Blinn-Phong model which includes an ambient term and it is based on that shiny surfaces have small intense specular highlights, while dull surfaces have significant highlights that fall off more gradually (5) [24].

$$L_r = \omega_d I_o \frac{\rho_d}{\pi} cos\theta_i + \omega_s I_o \frac{\rho_s}{\pi} \left(\frac{R}{\|R\|} \cdot \frac{V}{\|V\|}\right)^n \quad (5)$$

4.3 Unified Reflectance Model

Due to the Lambertian model is inaccurate in rough diffuse surfaces, we proposed to combine through a linear combination of Oren–Nayar model and the specular part of Blinn–Phong model (see Fig.4d)(6)[9].

$$L_r = \omega_d I_o \frac{\rho_d}{\pi} cos\phi_i \, (A + B \, max\,[0, cos\,(\theta_r - \theta_i)]\, sin\alpha tan\beta + \omega_s I_o \frac{\rho_s}{\pi} \, (n \cdot h)^n \quad (6)$$

5 3D IMAGE RECONSTRUCTION

The success of 3D image reconstruction based on the method of SFS depends greatly on the physical brightness surface and reflectance properties as well as the illumination conditions, and other extrinsic factors as camera properties (see Appendix B) and the reference coordinate system of the viewer/camera-centered. This method seeks to solve the image irradiance equation $E_r = R(n(x))$[25] where the normalized brightness $I(x)$ of gray-value image is related with the reflectance map $R(n(x))$. For 3D image reconstruction, we create a photo-metric image from a 2D low-resolution reconstructed image using a single-pixel with active illumination based on a Leds NIR array of 8x4 in the wavelength of 1550 nm in a rainy scenario (seen figure 5). The fact that our visual system has illumination active allows keeping a level of brightness not depend on the condition of the background light and rainy condition or scattering medium in the near-infrared present less attenuation than vision systems that work in the visible spectrum [6]. Using the 2D SPI-NIR image, the irradiance level is estimated E_r. Calculating the parameters albedoρ_d, θ_r and θ_i must be considering that a single light source of one direction L(sequence projection light using Hadamard pattern) with the image plane that coincides with the optical z-axis of the camera (detector single pixel), was used. Due to the relationship between the surface reflected radiance model L_r and the irradiance image E_r (2D image SPI-NIR), we can define $E_r = \eta L_r$[25] with that we can define irradiance image with information of depth (7).

$$I(x, y) = cos\phi_i \, (A + B \, max\,[0, cos\,(\theta_r - \theta_i)]\, sin\alpha tan\beta + (n \cdot h)^n \quad (7)$$

For solving (7), we can consider that the direction of the light source is the same as the camera, with that $\theta_i = \theta_r, \phi_i = \phi_r, \alpha = \theta_i = \beta$ and, $n \cdot h = cos\,(\theta_i)$, we can express irradiance image (9) [26] (see appendix B).

$$I\,(x, y)\sqrt{1 + \|\bigtriangledown z(x, y)\|^2} + \tilde{\omega} \cdot \bigtriangledown z(x, y) - \omega_s = 0, in\Omega \quad (8)$$

if we consider that source has one direction $\omega = (0, 0, 1)$ and (8) , it can be define as Eikonal equation [26](9).

$$|\bigtriangledown z(x, y)| = f(x), where f(x) = \sqrt{\frac{1}{I(x, y)^2} - 1} \quad (9)$$

6 EXPERIMENT AND RESULTS

To evaluate the 3D reconstruction vision system's capabilities with active illumination through the method of SFS with Eikonal solver (9) in rain condition, we develop a testing bench that has a controlled system of illumination to simulate background outdoor light and a system that can simulate the conditions of rain with a size drop of 0.5 mm,1 mm, and 2 mm (see Fig. 5.). For the 3D image reconstruction initially, we take a 2D image single-pixel NIR of low-resolution, which is obtained from 80% of the Hadamard patterns projected, and it is reconstructed through the technique of CS using the Batch algorithm in combination with the method of FSRCNN with upscaling factors of 4 [27] (see Fig.6 a,d). Due to the scattering effect caused by rain, a pre-process of the 2D SPI-NIR image was needed through Gaussian filter and morphologic methods before making the 3D image reconstruction using SFS. In this work, we focus on reconstructing objects with few details on their shape with rough surfaces in rainy conditions. For the first test, we reconstructed a homogeneous surface, for which we chose a bright spherical (a shape sphere object can be an ideal approximate of the Lambert surface and can be considered as a calibration object in the 3D reconstruction[25]) object of 50mm of diameter at a distance of between 10 to 17 cm from the focal lens (see Fig.6a) in which we applied scanning of the type basic and spiral. In the second test we reconstructed a rectangular area formed by a cube, its area is 40x40x40mm at a distance between 10 to 17 cm from the focal lens (see Fig.6d), and we applied a

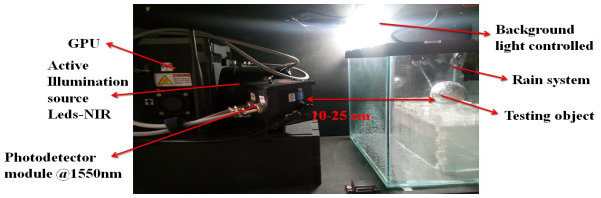

Figure 5: Experimental setup to vision system 3D SPI-NIR, the testing bench has a rain (size drop rain 0.5,1,2 mm) and background light-controlled system. Range of measuring between 10-25 cm (seen table I), the testing object must be positioned into the glass box to evaluate the performance of the 3D image reconstruction in rain conditions.

scanning basic and ZigZag. for the test, we used different scanning methods to determine which method can adapt better to rainy conditions depended on the type of surface that want to reconstruction.

6.1 Discussion: Testing 3D SPI-NIR reconstruction in rainy condition and without rain

In the tests carried out to 3D image reconstruction in rainy conditions, we define the measured distance between 10 to 17 cm, from the analysis of the modeling the SPI-NIR in condition rain (see table 2), the distance that is in the range of measure of an object with a high reflection index. In rainy conditions, for critical droplet sizes $< 1mm$ where the scattering effects are more, we can see a high level degradation of the quality of both objects' reconstructed 2D/3D image, the spherical object representing a more significant degradation. For the object, the square can see a degradation in the surface reconstructed due to attenuation and loss of information (see Fig.6f). If we applied a scanning method of the type Zig-Zag, it can improve the quality of 2D/3D image with a better level, $SSIM > 0.7$, compared to the basic scanning method. In the case of the reconstruction of the object with sphere shape in the test, we can see that the scanning method spiral have a better level SSIM in the rainy condition, and the 3D image has a high-level degradation for droplet sizes $0.5mm$ with a more significant loss of information (see Fig.6b,c) in comparison with a square object.About the processing time for reconstruction of sphere objects, the time is between 28 to 32 ms with the Hilbert scan as the lower, and Spiral as the faster, for case square object the time is between 27 to 30 ms, with the Basic scan being lower, and Zig-Zag is faster.

7 CONCLUSION

This paper presented a vision system SPI-NIR with active illumination of low resolution to 3D image reconstruction in rainy conditions for future application on in-vehicle UAVs. The 3D image reconstruction is based on the single-view methods shape-from-shading(SFS) with an Eikonal solver. In this work, first, we defined the measurement ranges by modeling the number of photons detected in the rainy condition (seen Appendix A Fig.7), and we can determine the effective measurement range between 10-28 cm (see table 2). Due to the scattering effect caused by the rain, the level of light reflected off the object will be attenuate, for which we proposed using a unified reflection model (6) to estimate 2D SPI-NIR image irradiance used to make the reconstruction 3D. In the test, we can see as the droplet size affect the quality of the 2D/3D image reconstructed. In the condition of fine drizzle with size droplet $< 1mm$, the scattering effect is more significant, so the 3D reconstruction has limitations. We implement different scanning methods for this as a solution depending on the type of element to detect. For example, in an urban ambient with many buildings, the 3D reconstruction is focused on detecting walls that can be approximate the reconstruction of an object with a shaped square. So the scanning ZigZag is a method more the most appropriate to make a 3D reconstruction. In contrast, in a scenario with more vegetation or mountains, we can approximate some scenario objects as shape spherical or curves, being a scanning Spiral method the most appropriate. This capacity to improve the quality of the 3D image increases the vision system's capabilities to applications to vehicles UMV in scenarios with rain.

REFERENCES

[1] Qinghua Huang and Zhaozheng Zeng. A review on real-time 3d ultrasound imaging technology. *BioMed Research International*, 2017:6027029, Mar 2017.

[2] Maged Aboali, Nurulfajar Abd Manap, Abd Darsono, and Zulkalnain Yusof. Review on three dimensional (3-d) acquisition and range imaging techniques. *International Journal of Applied Engineering Research*, 12:2409–2421, 06 2017.

[3] Fabian Wagner, Florian Schiffers, Florian Willomitzer, Oliver Cossairt, and Andreas Velten. Intensity interferometry-based 3d imaging. *Opt. Express*, 29(4):4733–4745, Feb 2021.

[4] Graham M. Gibson, Steven D. Johnson, and Miles J. Padgett. Single-pixel imaging 12 years on: a review. *Opt. Express*, 28(19):28190–28208, Sep 2020.

[5] Richard Hartley and Andrew Zisserman. *Camera Geometry and Single View Geometry*, page 151–152. Cambridge University Press, 2 edition, 2004.

[6] M. I. Mishchenko, L. D. Travis, and A. A. Lacis. *Multiple Scattering of Light by Particles: Radiative Transfer and Coherent Backscattering*. Cambridge University Press, Cambridge, 2006.

[7] J. Wojtanowski, M. Zygmunt, M. Kaszczuk, Z. Mierczyk, and M. Muzal. Comparison of 905 nm and 1550 nm semiconductor laser rangefinders' performance deterioration due to adverse environmental conditions. *Opto-Electronics Review*, 22(3):183–190, Sep 2014.

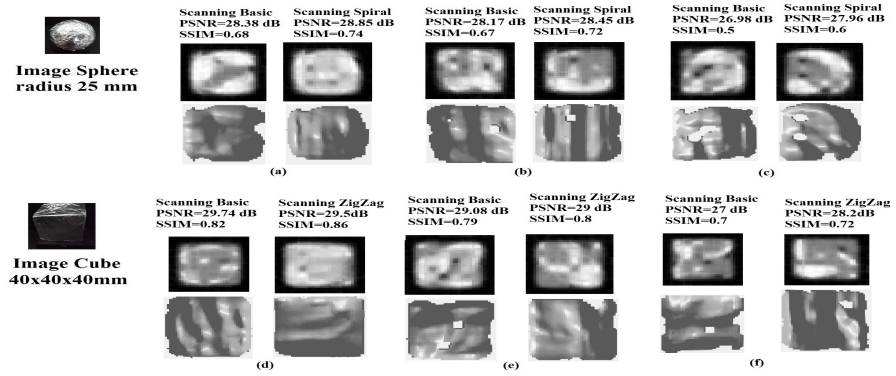

Figure 6: 3D SPI-NIR Image reconstruction with active illumination in wavelength of 1550 nm of a spherical object of 50mm diameter and cube object of 40x40x40mm both at a distance between 10 to 17 cm from the focal lens with a processing time of 28 ms and 32 ms respectively, we scanning basic and spiral to evaluate performance, we calculate the parameters PSNR and SSIM, a,d) without rain at 17 cm,b,e)in rainy conditions with a size drop diameter of 2mm at 15 cm,c,f) in rainy conditions with a size drop diameter of 0.5mm at 10 cm.

[8] Dragana Perić, Branko Livada, Miroslav Perić, and Saša Vujić. Thermal imager range: Predictions, expectations, and reality. *Sensors*, 19(15), 2019.

[9] Guohui Wang, Xuan Zhang, and Jin Cheng. A unified shape-from-shading approach for 3d surface reconstruction using fast eikonal solvers. *International Journal of Optics*, 2020:6156058, May 2020.

[10] Solar radiation photosynthetically active radiation. https://www.fondriest.com/environmental-measurements/parameters/weather/photosynthetically-active-radiation/. Accessed: 2021-01-28.

[11] R. Lange, S. Böhmer, and B. Buxbaum. 11 - cmos-based optical time-of-flight 3d imaging and ranging. In Daniel Durini, editor, *High Performance Silicon Imaging (Second Edition)*, Woodhead Publishing Series in Electronic and Optical Materials, pages 319–375. Woodhead Publishing, second edition edition, 2020.

[12] C. Osorio Quero, D. Durini, R. Ramos-Garcia, J. Rangel-Magdaleno, and J. Martinez-Carranza. Hardware parallel architecture proposed to accelerate the orthogonal matching pursuit compressive sensing reconstruction. In Lei Tian, Jonathan C. Petruccelli, and Chrysanthe Preza, editors, *Computational Imaging V*, volume 11396, pages 56 – 63. International Society for Optics and Photonics, SPIE, 2020.

[13] Lukas Roth, Andreas Hund, and Helge Aasen. Phenofly planning tool: flight planning for high-resolution optical remote sensing with unmanned areal systems. *Plant Methods*, 14(1):116, Dec 2018.

[14] Carlos Alexander Osorio Quero, Daniel Durini Romero, Ruben Ramos-Garcia, Jose de Jesus Rangel-Magdaleno, and Jose Martinez-Carranza. Towards a 3d vision system based on single-pixel imaging and indirect time-of-flight for drone applications. In *2020 17th International Conference on Electrical Engineering, Computing Science and Automatic Control (CCE)*, pages 1–6, 2020.

[15] Kuo-Nan Liou. An introduction to atmospheric radiation / kuo-nan liou., 1980.

[16] Matthew Lebsock and Tristan L'Ecuyer. The retrieval of warm rain from cloudsat. *Journal of Geophysical Research*, 116, 10 2011.

[17] Xiantong Liu, Qilin Wan, Hong Wang, Hui Xiao, Yu Zhang, Tengfei Zheng, and Lu Feng. Raindrop size distribution parameters retrieved from guangzhou s-band polarimetric radar observations. *Journal of Meteorological Research*, 32(4):571–583, Aug 2018.

[18] S-G. Park, V. N. Bringi, V. Chandrasekar, M. Maki, and K. Iwanami. Correction of radar reflectivity and differential reflectivity for rain attenuation at x band. part i: Theoretical and empirical basis. *Journal of Atmospheric and Oceanic Technology*, 22(11):1621 – 1632, 01 Nov. 2005.

[19] J. S. Marshall and W. Mc K. Palmer. The distribution of raindrops with size. *Journal of Atmospheric Sciences*, 5(4):165 – 166, 01 Aug. 1948.

[20] Jing Guo, He Zhang, and Xiang-jin Zhang. Propagating characteristics of pulsed laser in rain. *International Journal of Antennas and Propagation*, 2015:292905, Sep 2015.

[21] Ross Gunn and Gilbert D. Kinzer. The terminal velocity of fall for water droplets in stagnant air. *Journal of Atmospheric Sciences*, 6(4):243 – 248, 01 Aug. 1949.

[22] Matt Pharr, Wenzel Jakob, and Greg Humphreys. 08 - reflection models. In Matt Pharr, Wenzel Jakob, and Greg Humphreys, editors, *Physically Based Rendering (Third Edition)*, pages 507–568. Morgan Kaufmann, Boston, third edition edition, 2017.

[23] Michael Oren and Shree K. Nayar. Generalization of the lambertian model and implications for machine vision. *International Journal of Computer Vision*, 14(3):227–251, Apr 1995.

[24] Bui Tuong Phong. *Illumination for Computer Generated Pictures*, page 95–101. Association for Computing Machinery, New York, NY, USA, 1998.

[25] Fabio Camilli and Silvia Tozza. A unified approach to the well-posedness of some non-lambertian models in shape-from-shading theory, 2016.

[26] Silvia Tozza and Maurizio Falcone. Analysis and approximation of some shape-from-shading models for non-lambertian surfaces, 2016.

[27] Chao Dong, Chen Change Loy, and Xiaoou Tang. Accelerating the super-resolution convolutional neural network. *CoRR*, abs/1608.00367, 2016.

[28] Laser safety facts. https://www.lasersafetyfacts.com /laserclasses.html. Accessed: 2021-05-28.

[29] K. Garg and S.K. Nayar. Detection and removal of rain from videos. In *Proceedings of the 2004 IEEE Computer Society Conference on Computer Vision and Pattern Recognition, 2004. CVPR 2004.*, volume 1, pages I–I, 2004.

[30] Nicolas Hautière, Jean-Philippe Tarel, and Didier. Free space detection for autonomous navigation in daytime foggy weather. 05 2009.

[31] Emmanuel Prados and Olivier Faugeras. A generic and provably convergent shape-from-shading method for orthographic and pinhole cameras. *International Journal of Computer Vision*, 65(1):97–125, Nov 2005.

APPENDIX A: MODELING RAIN

A.1 Modeling SPI-NIR rain condition

The vision system proposed in this work is SPI-based [4], with illumination active for which we define as source light array LEDs of 8x4 that work in the wavelength of 1550 nm with a power level of 3.2W (IEC Eye Safety regulation IEC62471 [28]). The SPI-NIR system's critical factor is the minimum integration time T_{int} required by the photo-diode to capture the photons emitted by the array of LEDs to convert them into an electrical signal and above the background noise. This factor T_{int} determines the measuring maximum to reach outdoor by using (9)[14] that define the number of photons E(N) impinging the photo-detector photo-active in dry condition, and it depends on the spectral content $1544nm < \lambda < 1556nm$, the detector quantum efficiency $QE\left(\lambda\right)$ in this bandwidth, the length of the integration time of the detector T_{int}, and pixel's effective photo-sensitive area A_{pix}, defined as $A_{wxl}FF$, where A_{wxl} is the semiconductor window and FF the photodiode's fill-factor, $\Phi_{e\lambda}$ defined as the irradiation level of the active source, $E_{e\lambda\_sum(\lambda)}$ irradiation level of the sun illumination considered to be of 100 Klux, the $f_{\#}$ number define as $f_{\#} = f_{foc}/d_{aperture}$, f_{foc} is the length focal , and $d_{aperture}$ opening distance is the focal distance/opening distance, h is Planck's constant= $6.62607004x10^{-34}m^2kg/s$, z is the measured distance, c is the speed of light constant,τ the lens transmittance,ρ the material reflection index, and α_{FOV} the focal aperture angle [14] of the emitting LED array.

$$E(N) = \int_{\lambda_1}^{\lambda_2} \frac{\rho\tau_{lends} QE\left(\lambda\right) T_{int} A_{pix} FF\lambda}{hcf_{\#}^2} \left[E_{e\lambda\_sum(\lambda)} + \frac{\Phi_{e\lambda}}{\pi z^2 tan\left(\alpha_{FOV}\right)}\right] d\lambda \quad (10)$$

In rain condition, the irradiation level of the active source illumination is attenuate due to the scattering coefficient $\mu_s\left(\lambda, D\right)$ (11)[20] and absorption coefficient $\mu_a\left(\lambda, D\right)$(12)[20] relation of scattering Mie and weather parameters of rain environment model(seen figure 6) $\alpha\left(\lambda, D\right)$[20]. For which the distance of measure of the SPI system in scattering environment is less than to dry conditions (seen table I).To evaluate the effective measured range theoretical the (10) must consider the variables of the rain environment model proposed as $\alpha\left(\lambda, D\right)$[20], speed rain (13)[29] , the brightnesses of the dropping rain L_{r_i} and light of the background. Factors that affected the number of photons E(N) impinging the photodetector photoactive. The irradiation level of the active source (array LEDs) $\Phi_{e\ lambda}$ is attenuate a factor $\Phi_{e\lambda}e^{-\alpha(\lambda,D)z}$ and the $E_{e\lambda\_sum(\lambda)}$ of level background illumination is defined as $E_{e\lambda\_sum(\lambda)} = \left\lfloor \tau_{rain} AL_r + \tau_{rain}\left(1-A\right)L_b + \left(T_{patterns} - \tau_{rain}L_b\right)\right\rfloor$ [30] ,where $L_{r_i} = L_{r_{i-1}}e^{-\beta z} + L_b\left(1-e^{-\beta z}\right)$ [30] and the brightness level of the background light received by the detector is affected by the speed of the raindrops and the projection time of the projected Hadamard light patterns, as a gain factor of the received light we have the variable $A = \frac{\pi f_{foc}^2 D^2}{z}$ which corresponds to focal parameters of our system, the β variable is defined as a geometric factor of the raindrop $0 < \beta < \frac{\sqrt{D}}{50T_{patterns}}$[29].

$$\mu_s\left(\lambda, D\right) = \int \sigma_s\left(\lambda, D\right) N(D) dD \quad (11)$$

$$\mu_a\left(\lambda, D\right) = \frac{\pi D^2}{4} Q_{abs}\left(\lambda, D\right) \quad (12)$$

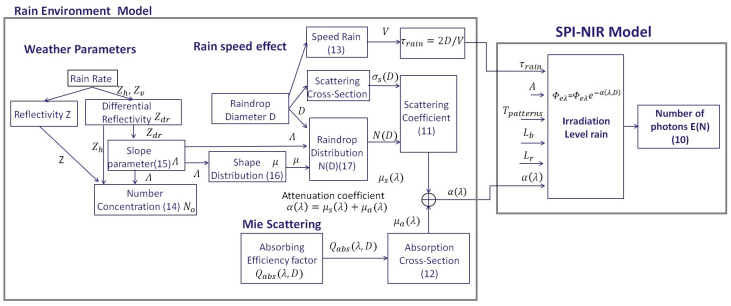

Figure 7: Overall block diagram single-pixel rain environment model proposed, we considered weather parameters, Mie Scattering,absorption efficiency Q_{abs}[20], speed dropping rain,raindrop distribution $N(D)$[20], concentration rain N_o[17], slope concentration distribution Λ[17],shape parameter μ[17], and SPI-NIR model to evaluate the range detection practical theoretical of the detector InGaAs (1550 nm).

$$v = -0.1021 + 4.932D - 0.9551D^2 + 0.07934D^3 - 0.002362D^4 \quad (13)$$

$$N_o = Z_h 10^{\left(0.00285Z\Lambda^3 - 0.0926\Lambda^2 + 1.409\Lambda - 3.764\right)} \quad (14)$$

$$\Lambda = 0.0125{Z_{dr}}^{-3} - 0.3068{Z_{dr}}^{-2} + 3.3830{Z_{dr}}^{-1} + 0.179 \quad (15)$$

$$\mu = -0.0201\Lambda^2 + 0.902\Lambda - 1.718 \quad (16)$$

$$N(D) = N_0 D^{\mu} e^{-\Lambda D} \quad (17)$$

APPENDIX B: INTRINSIC MATRIX AND EIKONAL SOLVERS

B.1 Intrinsic Matrix

The intrinsic matrix of the vision system SPI is defined using the model Pinhole with a focal length 25 cm,and axis skew, s=0 (18)[31].

$$K = \begin{bmatrix} f_x & s & x_0 \\ 0 & f_y & y_0 \\ 0 & 0 & 1 \end{bmatrix} = \begin{bmatrix} 114 & 0 & 90 \\ 0 & 114 & 100 \\ 0 & 0 & 1 \end{bmatrix} \quad (18)$$

B.2 Unified Eikonal-Type PDE Equation

For method, SFS we define a 3D surface as a projection of the first partial derivatives of the surface z(x, y) with respect to x(19)[25] and y(20)[25] with a vector n(21)[25] normal of the surface point.

$$p(x,y) = \frac{\partial z(x,y))}{\partial x} \quad (19)$$

$$q(x,y) = \frac{\partial z(x,y))}{\partial y} \quad (20)$$

$$n(x,y) = \frac{(p,q,-1)}{\sqrt{1 + \|\bigtriangledown z(x,y))\|^2}} \quad (21)$$

if we considered that the direction of light source L is the same as the camera direction V, the irradiance image equation (7) defined as (22), for $\omega_s = 0$ (22) can be define as (8) and solver using (9), for the unified reflectance $\omega_s \neq 0$, needs to apply the Newton–Raphson method (23) [9] using the definition (26), as strategy to accelerate the calculations we applied the fast eikonal solvers based on the numerical method of Godunov-Based [9].

$$I(X,y) = \omega_d \left(\frac{A}{\sqrt{1 + \|\bigtriangledown z(x,y))\|^2}} + \frac{B \bigtriangledown z(x,y)^2}{1 + \|\bigtriangledown z(x,y)\|^2} \right) + \omega_s \left(\frac{1}{\sqrt{1 + \|\bigtriangledown z(x,y)\|^2}} \right)^n \quad (22)$$

$$|\bigtriangledown z(x,y)| = \sqrt{\frac{1}{(T^k)^2} - 1}, \forall (x,y) \varepsilon \Omega, where$$
$$T = \frac{1}{\sqrt{1 + \|\bigtriangledown z(x,y))\|^2}} \quad (23)$$

For solving (23), we must be defined (22) as (24) and its first derivate(25)[9].

$$F(T) = \omega_s T^n - B\omega_d T^2 + A\omega_d T + B\omega_d - I \quad (24)$$

$$F^{'}(T) = n\omega_s T^{n-1} + \omega_d \left(A - 2BT\right) \quad (25)$$

$$T^k = T^{k-1} - \frac{F(T^{k-1})}{F^{'}(T^{k-1})} \quad (26)$$